Alcanivorax borkumensis Biofilms Enhance Oil Degradation By Interfacial Tubulation

ONE SENTENCE SUMMARY

A. borkumensis adapt their interfacial properties over time to evolve their biofilm phenotype and increase their oil consumption

AUTHORS

M. Prasad[1], N. Obana[2,3], S.-Z. Lin[4], K. Sakai[5,6], C. Blanch-Mercader[7], J. Prost[7,8], N. Nomura[1,3], J.-F. Rupprecht[4*], J. Fattaccioli[5,6*], A. S. Utada[1,3*]

AFFILIATIONS

[1]Faculty of Life and Environmental Sciences, University of Tsukuba, 1-1-1 Tennodai, Tsukuba, Ibaraki 305-8572, Japan
[2]Transborder Medical Research Center, Faculty of Medicine, University of Tsukuba, 1-1-1 Tennodai, Tsukuba, Ibaraki 305-8575, Japan
[3]Microbiology Research Center for Sustainability (MiCS), University of Tsukuba, 1-1-1 Tennodai, Tsukuba, TARA center, Ibaraki 305-8572, Japan
[4]Aix Marseille Université, Université de Toulon, CNRS, Centre de Physique Théorique, Turing Center for Living Systems, Marseille, France
[5]PASTEUR, Département de Chimie, École Normale Supérieure, PSL Université, Sorbonne Université, CNRS, 75005 Paris, France
[6]Institut Pierre-Gilles de Gennes pour la Microfluidique, 75005 Paris, France
[7]Laboratoire Physico-Chimie Curie UMR168, Institut Curie, Paris Sciences et Lettres, Centre National de la Recherche Scientifique, Sorbonne Université, 75248 Paris, France
[8]Mechanobiology Institute, National University of Singapore, 117411 Singapore

Correspondence: utada.andrew.gm@u.tsukuba.ac.jp, jacques.fattaccioli@ens.psl.eu, jean-francois.rupprecht@univ-amu.fr

ABSTRACT

Alcanivorax borkumensis are prominent actors in oil spill bioremediation; however, the interfacial dynamics of their biofilms and its role in oil degradation remain unclear. Longitudinal tracking of biofilm-covered oil microdroplets using microfluidics reveals a spontaneous morphological transition from a thick biofilm phenotype to a thin dendritic phenotype optimized for high oil consumption rates. We show experimentally that biofilm dendrites emerge from aster-like nematic defects in the thin biofilms. We develop a theoretical model that elucidates the transition between phenotypes, linking tubulation to decreased interfacial tension and increased cell hydrophobicity, which we verify experimentally. We demonstrate positional control over the nematic defects on the droplets using microfluidics, causing the biofilm to dimple the droplets. Our results reveal how *A. borkumensis* biofilms utilize topological defects to increase oil access to achieve superior oil consumption rates, which may be a general strategy in oil-consuming bacteria.

KEYWORDS

Alcanivorax borkumensis; Oil bioremediation; Microfluidics, Confined Nematic Ordering, Collective Behavior; Contact angle; Cell-surface Hydrophobicity

INTRODUCTION

Obligately hydrocarbonoclastic bacteria (OHCB) are a group of cosmopolitan marine bacteria with an unusual ecology: they can survive by consuming hydrocarbons as a sole energy and carbon source (*1*). In the marine environment, these bacteria are typically found at very low densities but can bloom to become the dominant bacteria at the site of oil spills (*1*, *2*). They are thought to degrade a significant amount of the worldwide spilled oil (*3*–*5*), which has generated interest in these organisms for their technological potential as agents of bioremediation (*5*–*8*).

Alcanivorax borkumensis SK2 was the first hydrocarbonoclastic bacteria whose genome was sequenced and is frequently used as a model OHCB (*6*, *9*). Like most bacteria, it transitions between a free-living lifestyle to one as part of a social collective, called a biofilm, which is now recognized as integral to bacterial biology (*10*, *11*). Most biofilms are 3-dimensional communities of densely packed cells that cooperatively secrete extracellular polymeric substances (EPS) that both protect and help the community remain attached to solid surfaces (*12*). This high cell density creates gradients where outward-facing cells have greater access to important nutrients than cells in the interior. However, unlike most biofilm-forming bacteria, *A. borkumensis* form biofilms at the oil-water, a liquid-liquid interface; here, the formation of biofilm creates opposing gradients in the access to oil relative to nutrients needed for respiration. How these nutritive gradients and the fluid nature of the interface affects OHCB biofilm formation and oil consumption remains largely unexplored.

Most knowledge of bacteria-mediated oil degradation comes from genomic sequencing and metagenomic assays (*6*, *13*, *14*), mutant screens (*15*), interfacial rheology (*16*–*18*), and microcosm tests (*13*, *19*, *20*). However, a comprehensive picture of the mechanism of biofilm formation and its coupling to oil degradation remains unclear. To date, few studies have focused on the dynamics of OHCB biofilms formation at the oil-water interface at the micro-drop scale (*21*–*23*). Nonetheless, these studies do not resolve the physical process of biofilm formation and oil degradation at the single-bacterium scale.

To address these questions, we developed a microfluidic device that allows the trapping and real-time imaging of numerous bacteria-covered oil droplets; this platform allows us to capture the full dynamics of biofilm development starting from individual bacteria through the complete consumption of oil droplets. We show that *A. borkumensis* presents distinct biofilm phenotypes that correlate with culture time using oil. For short culture times, they present as a thick, spherical biofilm (SB) that envelops the droplet. For long culture times, they present as a thin, dendritic biofilm (DB) that stretches and tubulates the drop interface, leading to rapid consumption. We show that tubulation is initiated at aster-like topological defects found in the nematic order of interfacial cells. Using a coarse grain model to describe the biofilm dynamics, we predict that the balance between cell density, interfacial tension, and cell hydrophobicity facilitates a rapid, exponential-like stretching of the interface and confirm this experimentally. Ultimately, the capacity for tubulation at the oil-water interface could be a factor leading to the blooming of *A. borkumensis* after oil spills.

RESULTS

Experimental setup and microfluidic device

In pristine marine environments, *A. borkumensis* primarily uses water-soluble organic acids, such as pyruvate, as its carbon and energy source. During marine oil spills, they transition to using water-insoluble alkanes. To study the biofilm dynamics after this transition, we initially cultivate the bacteria using pyruvate, and then switch to a minimal medium supplemented with hexadecane (C16), where we incubate for up to 5 days (d) (**Fig. S1A** and **Supplementary Information (SI) - Methods** section). Using these cultures, we periodically sample the bacteria by generating cell-laden oil microdroplets with fresh C16, which we store in individual traps in our microfluidic platform (*24*). Our device facilitates *in situ* culturing, which enables the longitudinal investigation of biofilm development on specific droplets (**Fig. 1A**, **Fig. S2A,** and **SI - Microfluidics**). Drops imaged immediately after being trapped initially have ~20-50 cells attached (**Fig. S3A**). These cells divide to form a confluent monolayer over the course of ~12 h. We define the t_0 of our experiments as the moment of confluency.

Bacteria exhibit two distinct phenotypes and consumption rates

Sampling bacteria over 5 d reveals different phenotypes that manifest vastly different biofilm morphologies and oil consumption rates. When sampled after 1 d, *A. borkumensis* form a spherical biofilm (SB) that grows outward from the oil; here, the oil droplet remains spherical as it is consumed **(Fig. 1B, Fig. S3B, and Movie S1)**. In striking contrast, bacteria sampled from 5 d culture can develop into thin biofilms with a local nematic ordering of the interfacial cells, which eventually buckle and then tubulate the droplet interface, as shown in **Fig. 1C**; we call these dendritic biofilms (DB). In this case, the biofilm buckles the interface to accommodate a population that is continuously increasing in

number. The magnitude of the deformations grows as the oil is consumed, which ultimately shreds the droplets into tiny fragments (**Fig. S3C and Movie S2)**.

We quantify the oil consumption rate for each phenotype by measuring the droplet volume (V) from brightfield and confocal images of the droplet surface area (S) over time (**SI - Methods**). SBs consume >90% of the initial volume in ~72 h, whereas DBs achieve the same in ~20 h. We find that the oil volume of SBs decreases as a polynomial function of time, whereas for DBs, the decay is much faster (**Fig. 1D,E** and **SI - Eq.11**). In both cases, the decrease is consistent with a model of oil consumption effected exclusively by bacteria at the interface (**SI - Analytical Model of Oil Consumption**).

The good agreement between our analytical models and data allows us to estimate the per-cell consumption rates of both SB and DB cells as 0.7 and 0.8 fL/h, respectively; this small difference in consumption rate is consistent with their similar division times (**Fig. S1D**). For comparison, the volume of a single cell is ~1 fL, meaning that these bacteria consume a volume of oil close to their own, every hour. Despite the similarity in consumption rates on a per-cell basis, the normalized surface-to-volume ratio (S^*/V^*) shows that DBs are significantly more efficient: S^*/V^* doubles in 72 h for SBs, whereas it diverges in less than 24 h for DBs (**Fig. 1E, inset**). The S^*/V^* ratio provides a means for comparing the relative efficiencies of the two phenotypes and highlights the fact that these differences arise from the rapid increase in interfacial area caused by DB biofilms. In both cases, the shape of the interface defines the dynamics of volume decrease. For SBs, the interfacial area defined by the spherical droplet determines the number of cells (N) that can pack onto the interface to have access to the oil. Conversely, for DBs, it is the increase of N at the interface due to cell division that determines the interfacial area. Thus, the rate of consumption decreases over time for SBs, while it increases continuously for DBs.

Tubulation is facilitated by topological defects

We correlate the onset of the rapid increase in surface area for DBs to the emergence of nematic order of the interfacial cells. Numerous examples have shown that rod-like bacteria can locally align in the same direction, defining a nematic order field (*25–28*). Active systems with nematic order have demonstrated the ability, both in theory (*29*, *30*) and in experiments (*31–34*), to utilize topological defects to achieve surface deformation. Here, at 2-4 h post-confluency, we observe the appearance of conical protrusions of cells that originate from the core of aster-like (+1) topological defects within the nematic field (**Fig. 2A,B** and **Fig. S4A,B)**. As the biofilm matures, more protrusions appear while existing protrusions elongate into branched bacteria-covered tubes (**Fig. 1C (16 h)** and **Fig. 2C)**.

Differential labeling of the oil and cells reveals that the tubes are not filled with water; instead, they are filled with oil (**Fig. S5A**). This result indicates that cell adhesion to the oil stabilizes the tubes

158 against collapse, thereby preventing the deformed droplet from regaining a spherical shape.
159 Furthermore, careful inspection of the confocal images of the tubes reveals that the bacteria are well
160 aligned to the tube axis, which becomes clear in the orientation director field of the cells on the tube
161 (**Fig. 2D**). We characterize cell alignment along the tube by calculating the local average scalar
162 product between the director field and the tube axis, finding values close to 1 along the tube; this
163 indicates that the cells are highly aligned with the tube axis (**Fig. 2E, Fig. S5B and C,** and **SI -**
164 **Methods**).
165
166 Due to this parallel alignment of cells on the tubes, we hypothesize that the rate of increase of the
167 tube length is proportional to the number of cells on the tube, which should increase exponentially if
168 all cells were to divide. We measure tube elongation on different droplets, finding that it increases
169 rapidly and in a manner consistent with exponential elongation, supporting this hypothesis (**Fig. 2F**,
170 **Fig. S5D**, and **SI-Methods**). Furthermore, from the fit to our data, we extract a tube length-doubling
171 time of ~3.4 h, which is 2-fold larger than the cell division time (t_{div}) of 1.65 h (**Fig. S1D**). This difference
172 likely arises from the imperfect alignment of cells along the tubes and from the expulsion of cells from
173 the tube interface during elongation, which is visible around the tubes (**Fig. 2C**).
174
175 **Biofilm phenotypes are associated with a decrease of interfacial tension**
176 The large difference in biofilm morphology between the two phenotypes suggests differences in their
177 interfacial properties. *A. borkumensis* are known to secrete biosurfactants both on the cell surface
178 and into the environment, which are thought to aid in the assimilation of oil (*9*, *35*). These
179 biosurfactants can lower the oil-water interfacial tension (γ), making it easier to deform the interface,
180 and form conditioning films at interfaces, which can facilitate surface colonization. To measure
181 differences in interfacial properties based on biofilm phenotype, we fractionate SB and DB cultures
182 into three components: cells, conditioned media, and conditioned C16 to independently measure γ
183 for each (**Fig. S6A**). We find that γ for each of the respective fractions are depressed relative to
184 control values; however, the DB-conditioned oil decreases the most. The γ for DB-conditioned oil
185 decreases from 30 to 8 mN/m and is about half the value for SBs (**Fig. 3A, Fig. S6B-D** and **Table**
186 **S1**). Surprisingly, when we microfluidically "re-sample" the biofilm phenotype using the DB-
187 conditioned C16 instead of fresh C16, we find no change in observed phenotype (**Fig. S6E**). Thus,
188 despite the ~4 fold lower γ of DB-conditioned oil, the SB cells are unable to deform the oil-water
189 interface, indicating that a lower γ is not sufficient to produce the DB phenotype.
190
191 Interfacial behavior is also affected by cell hydrophobicity, which, together with γ controls the extent
192 to which cells are wetted by the oil (**Fig. S7A**). Cell hydrophobicity is thought to increase the longer
193 cells consume oil, however the relationship with phenotype is unclear (*20*, *36*). Although the bacteria

194 appear to lay flat on the surface at t_0, the microscopic contact angle is difficult to estimate from
195 confocal images (**Fig. S7B)**. Thus, to estimate hydrophobicity for the cells of both phenotypes, we
196 measure the 3-phase contact angle (θ) between water that we deposit on a bacterial lawn submerged
197 in oil (*37*) (**Fig. S7C-E** and **SI-Methods**); θ=90° is the neutral wetting condition and larger θ's indicate
198 greater hydrophobicity. SB cells, which are isolated after 1 d of culture, have a θ≈80°, whereas DB
199 cells, which are isolated after 5 d, have a θ≈100° (**Fig. 3B** and **SI-Methods**). This indicates that the
200 midplanes of SB and DB cells are ±10% above and below the interface, respectively (**Fig. S7A**).
201
202 The higher hydrophobicity of DB cells indicates that they have a larger interfacial adhesion strength
203 than SB cells. To directly compare the respective adhesion strengths of SB and DB, we force them
204 to compete for interfacial area on oil microdroplets, noting that both phenotypes have similar division
205 times (**Fig. S1D**). We generate cell-laden droplets using mCherry-expressing SB cells and GFP-
206 expressing DB cells in a 3:1 ratio, and record fluorescence intensity as the biofilm develops. Since
207 the same oil substrate is used, we ensure that both phenotypes experience the same γ. We find that
208 although the DB cells are initially in the minority, they gradually displace the established SB, to
209 become dominant in ~5 h (**Fig. 3C,D**). This result confirms our expectation that DB cells, which are
210 more hydrophobic do indeed have a larger adhesion energy to the interface than SB cells.
211
212 Rod-shaped gammaproteobacteria like *Pseudomonas aeruginosa* have been shown to colonize and
213 remodel oil-water interfaces with their biofilms, similar to what we observe in the early stages (<3 h)
214 of DB formation (*17*, *18*). However, those biofilms lack the large-scale deformations that we observe
215 in later stages of DB formation (**Fig. 1C**, >5 h). From our measurement of the oil-water interfacial
216 tension, the biofilm compression modulus is estimated to be ~200 Pa (*38*), which is much smaller
217 than the ~1 MPa extensional growth pressure of *P. aeruginosa* (*39*). Assuming that *A. borkumensis*
218 have a similar growth pressure, cell division supplies enough stress to easily deform the interface.
219 Thus, DBs generate the biofilm phenotypes we observe only if a sufficient number of cells remain
220 adhered to the interface to drive the tubulation process. Conversely, the lack of deformations in the
221 SB phenotype is the consequence of cell detachment from the interface followed by biofilm formation
222 around the droplet.
223
224 **Membrane theory predicts the transition from SB to DB phenotype**
225 Based on these observations, we develop a coarse-grain membrane model to describe the interfacial
226 dynamics of the growing interfacial biofilm. The model explains the transition between SB and DB
227 phenotypes in terms of a competition between the interfacial tension and the spontaneous curvature
228 of the biofilm, which is its intrinsic tendency to bend in a preferred direction. Interfacial tension resists
229 expansion of the surface by the biofilm, while the spontaneous curvature of the biofilm governs the

shape of the expanding surface. When the energetic cost of increasing surface area is lower than the cost of bending, tubes are generated, which expand exponentially according to the following equation:

$$\eta \frac{1}{L}\frac{dL}{dt} = -\left(\sigma_{t,H} + \sigma_{n,H} - \frac{\kappa_B}{r_0 r_{\mathrm{eq}}}\right), \qquad \text{Eq. (1)}$$

where L is the tube length, η is the viscosity of the biofilm layer, $\sigma_{t,H}$ and $\sigma_{n,H}$ are the respective tensions along the circumferential and normal directions of the tube, κ_B is the bending rigidity of the membrane in the circumferential direction of the tube, $1/r_0$ is the spontaneous curvature of the biofilm, and r_{eq} is the tube radius (**SI – Membrane Model** and **Fig. S14**).

Eq. 1 encompasses the existence of active extensile nematic stresses driven by bacterial growth, with an effective interfacial tension $\gamma_{eff}(\rho) = ½(\sigma_{t,H} + \sigma_{n,H})$ that depends on the interfacial cell density ρ (**SI – Membrane Model**). This implies that tubulation occurs at a critical buckling density (ρ_B), consistent with our observation that tubes form after confluency (**Fig. 1C**). In our model, bacteria populate a circular oil-water interface with a density that increases logistically towards a homeostatic density (ρ_H), where division and loss are balanced. Depending on the ratio ρ_B/ρ_H, the phenotype changes: when $\rho_B/\rho_H > 1$, tubes are unable to form, resulting in the SB phenotype; when $\rho_B/\rho_H < 1$, the interface buckles and stable tubes form, producing the DB phenotype. Our model implies that physically lowering ρ by removing cells of a DB below the critical value should cause a deformed droplet to recover its unperturbed spherical shape. To test this hypothesis, we expose DBs to a flowing surfactant mixture to disrupt the biofilm (**SI - Methods**). Following a ~4 h lag, the biofilm abruptly washes away and the deformed droplets become spherical; this recovery is the consequence of positive interfacial tension in the absence of bacteria (**Fig. S8A,B** and **Movie S3**).

In addition to the SB and DB phenotypes described so far, we observe an intermediate phenotype when we isolate cells at an intermediate culture time (**Fig. S1A**). These biofilms present dynamic oscillatory behavior (OB), alternating between the dendritic and spherical biofilms, with a period of ~12 h (**Fig. 3E**, **Fig. S9,** and **Movie S4**). The relatively short (~30 min) transition from tubulated to spherical is consistent with a sudden loss of tube stability, which, based on **Eq. 1**, is consistent with a sudden increase in the effective surface tension.

To elucidate the emergence of oscillations between spherical and dendritic phenotypes, we use a phase-field approach following an established literature on simulating interfacial dynamics of multiphasic systems (*40*). In our case, the simulated field is the local fraction of oil (φ(x,y)) that obeys a Cahn-Hilliard equation with an interfacial term $\kappa_1(\rho)(\nabla\varphi)^2/2$; here, $\kappa_1(\rho)$ is defined by right hand side of **Eq. 1** and sets the tube elongation rate. $\kappa_1(\rho)$ is thus a proxy for the active stress along the interface (**SI - Membrane Model**). In our model, a linear relation of the form $\kappa_1(\rho) = \gamma - k_1\,\rho$, where k_1 accounts

for the force exerted by the biofilm on the oil is sufficient to understand the SB-to-DB transition. The interface remains spherical until ρ surpasses the critical density, $\rho_B = \gamma / k_1$; here, $\kappa_1(\rho)$ becomes negative and tubulation occurs as the interface buckles. However, the morphological oscillations emerge only if we consider a second-order expansion of $\kappa_1(\rho)$ in ρ, such that an 'optimal' cell density exists where tube elongation and the final tube length are maximal, which we denote ρ_S (**Fig. 3F**). Oscillations arise for the specific case when $\rho_B<\rho_S<\rho_H$ (**SI - Phase-Field Model**); here, as cell density increases beyond the optimal value ρ_S, tube elongation ceases, and contraction starts. During this contraction, the surface shrinks faster than cells can be ejected from the interface, leading to an abrupt increase in bacterial density. We find that ρ overshoots ρ_H and causes $\kappa_1(\rho)$ to become positive (**Fig. 3F, blue**). This dynamical overshoot ultimately induces a catastrophic collapse of the tubes and is accompanied by a large reduction in the number of cells at the interface. Consistent with this prediction, in our experiments we observe a large and persistent flow of cells away from the interface soon after tube collapse (**Movie S4**). Our biomechanical model recapitulates the transition from these three phenotypes in terms of a tubulation mechanism that depends on bacterial growth dynamics, with oscillations emerging through a dynamical phase transition mechanism (*41*) (**Fig. 3G, Movie S5**). These oscillations are driven by continuous cell division that pushes density beyond the critical values for tube growth and collapse.

Controlled Buckling of Confined Droplets

We leverage microfluidics to position the topological defects that generate tubes by controlling the shape of the trapped drops. By using droplets whose diameters are larger than the trap height, we can generate biofilms on drops that are flattened by the trap ceiling (**Fig. 4A - Upper inset)**. These flattened circular faces allow us to position the nematic defects in the center, which concentrates growth stress and thereby generates centrally located dimples. Unlike smaller drops, which are uniformly covered with a bacterial monolayer, interfacial tension initially excludes bacteria from the flattened regions on large drops (**Fig. 4A** and **Fig. S10(A-B)**). At a critical cell density, bacterial growth pressure enables cells to invade the flat regions, which they do so isotropically (**Movie S6**). Once confluency is reached, the nematic field displays an aster-like +1 defect (or two closely spaced +1/2 defects) in the center, as expected from liquid crystal theory (*42*, *43*) where flows orient the cell nematic director (**Fig. 4B** and **Fig. S10(C-D)**). As cell division continues, we observe the formation of a large dimple at the defect, which grows inward into the droplet (**Fig. 4C** and **Fig. S10E)**. By symmetry, a similar process occurs at the top of the drop (**Fig. S10B-inset**). We find that the height profile of the dimple agrees with a model of spontaneous deformation of a liquid crystalline membrane with a radial nematic order (*30*, *44*), given by:

$$h = h_0 \int_R^r K\left(\sqrt{1-\frac{\kappa_F}{\kappa_B}}, \frac{r'}{\sqrt{\kappa_B/\gamma}}\right) dr' \quad \text{Eq. (2)}$$

where h is the dimple height, r is the radial position, R is the radius of the dimple, $K(\alpha,x)$ is a modified Bessel function of order α, and κ_F is the elastic constant of the nematic director field (see **SI – Fitting Procedure**). The theoretical profiles depend on a scaling factor h_0 and the two dimensionless parameters κ_F/κ_B and $\kappa_B/\gamma R^2$; these parameters arise from the competition between the Frank free energy and the bending energy, and between the bending energy and the surface tension, respectively. Our fitting procedure yields a ratio $\kappa_F/\kappa_B \approx 2$, highlighting the prominent role of the bacterial nematic order on the dimple profile (**Fig. S12**). In agreement with experiments, the profiles in this parameter regime are qualitatively similar to pseudospheres (**Fig. 4D** and **Fig. S13**). The rounded shape at the inward tip is a consequence of the finite size of the bacteria, which have non-zero bending moduli.

DISCUSSION

Although bacteria are known to play an integral role in the bioremediation of spilled oil, the microscopic mechanism of how hydrocarbonoclastic marine bacteria engage and break-down oil remains largely unexplored. The process of biodegradation has been studied using *in situ* microcosm tests and batch reactors, which cannot reveal the underlying physics at the oil-water interface. To circumvent the vagaries of bulk and average measurements, we leverage oil-drop microfluidics to enable simultaneous longitudinal tracking of numerous individual oil-consuming biofilms, at unprecedented spatial and temporal resolution. By sampling *A. borkumensis* cells from cultures that have been adapted to metabolizing oil for variable durations, we show that the expressed phenotype depends on the culture duration and is more complex than previously known. Cells adapted for oil consumption possess the ability for explosive growth, generating biofilms that are morphologically distinct from biofilms formed from less-adapted cells.

We explain the appearance of this optimized phenotype by linking it to measurable increases in cell hydrophobicity and interfacial adhesion, which correlate to cultivation time with oil. These optimized cells collectively manipulate the shape of their carbon source to substantially increase the number of cells that may simultaneously feed; this greatly increases the rate of oil consumption. And, although 'higher' organisms enact similar food-reshaping activities (*45*), to the best of our knowledge this type of cooperative behavior is unique in bacteria. Surprisingly, at the single-cell level, the optimized cells are no more efficient at consuming oil than are their unoptimized counterparts, despite their considerably more efficient biofilms. Taken together, this increase in efficiency may be one factor,

among many, that leads to the observed blooms of *A. borkumensis* and other similar organisms after oil spills (*46*).

The high spatio-temporal imaging of numerous optimized biofilms afforded by our platform, further reveals the mechanism of their interfacial manipulation: as cell density increases past confluency, the biofilm buckles at aster-like defects in the nematic field, allowing the cells to escape the confines of the droplet surface. Importantly, rather than peeling away from the oil, the biofilm protrusions entrain oil as they elongate into tubes. Recent developments on defect-driven morphogenesis have highlighted the importance of defects in the nematic order (*26*, *28*, *30*, *32*, *33*). We show indeed that *A. borkumensis* biofilms utilize nematic defects to enact topological deformations of the interface that results in exponentially elongating tubes, generating new surface area where more cells may feed. Thus far, models of oil biodegradation have treated droplets as shrinking spheres. Here, we develop an active matter theory to capture the dynamics of tube formation based on the most recent development of active nematics on curved geometries (*47*). Our model recapitulates each phenotype and can explain the existence of the striking oscillations in the biofilm morphology. Since we obtain OB cells at intermediate adaptation times, these cells may present an intermediate hydrophobicity. It will be interesting to explore whether a coupling between growth and competition for resources between un- and partially-adapted cells drives the oscillatory behavior (*48*).

In one set of experiments, we show that addition of surfactants that mimic oil-dispersant formulations to the culture medium leads to rapid biofilm detachment from the oil; this uncoupling abruptly halts oil consumption. Other than screening for enrichment of specific microorganisms in microcosm tests (*13*), to our knowledge, there is no experimental way to directly assess how medium composition affects oil-degradation by OHCB, despite the practical importance of this question. Our result clearly shows that surfactants can significantly affect biofilm formation; however, in the environment, many factors can possibly affect the final community composition, such as nutrient concentration, surfactant dilution, the specific mechanism of interfacial adhesion by different microbial species, and surfactant tolerance. Thus, how surfactants shape OHCB biofilm development remains an open question.

Application of this method to analyze other OHCB species could begin to provide information that complements metagenomic screens and could serve as a starting point to investigate how OHCB behave under different conditions. Our microfluidic platform is sufficiently general to accommodate studies of the population dynamics of both mono- and mixed-cultures of oil-consuming microorganisms subjected to different oil substrates, culture conditions, and different oil-dispersants. Results from such tests could provide insight into improving current remediation procedures in the field ranging from guidance on the suitability of a specific OHCB to a particular environment, to the potential of pre-adapting organisms of interest to local conditions to accelerate bioremediation.

CONTRIBUTIONS

MP, NO, KS performed the experiments; MP, NO, NN, JF, ASU analyzed and discussed the data; CBM, JP, JFR, SZL designed the tubulation theory; SZL carried out simulations; CBM performed the dimple height analysis; MP, CBM, NO, JFR, JF, ASU wrote the manuscript; JF and ASU conceived of the project.

ACKNOWLEDGMENTS

We thank Y. Yamashita (UT) for use of the contact angle/pendant drop systems, F. Pincet (Laboratoire de Physique, ENS) for assistance with micropipette experiments, D. Quéré (ESPCI) for the fruitful discussion on the O/W/cell contact angle measurements, and F. Brochard-Wyart (Institut Curie) for discussions on tube formation.

FUNDING

The research leading to these results was supported by the JSPS–ANR SAKURA Grant (JF, ASU, NO), JSPS BRIDGE Fellowship (JF), JST-ERATO (NN) (JPMJER1502), JSPS Kakenhi B (ASU) (21H01720), France 2030 (ANR-16-CONV-0001) (JFR), Excellence Initiative of Aix-Marseille University - A*MIDEX (JFR) and ANR-20-CE30-0023 (JFR).

COMPETING INTERESTS

The authors declare that they have no competing interests.

DATA AND MATERIALS AVAILABILITY

All materials are available upon request.

SUPPLEMENTARY MATERIALS

Supplementary Information:

- Materials And Methods,
- Analytical Model of Oil Consumption
- Extended Tubulation Model
- Fitting Procedure for the Dimple Profiles
- Supplementary Figures: Fig S1-S17
- Supplementary Tables: Table S1-S2
- Supplementary Movies: Movie S1-S6

405 ● Supplementary References (*1-29*)

REFERENCES (Main Text)

1. I. M. Head, D. M. Jones, W. F. M. Röling, Marine microorganisms make a meal of oil. *Nat. Rev. Microbiol.* **4**, 173–182 (2006).

2. Y. Kasai, H. Kishira, T. Sasaki, K. Syutsubo, K. Watanabe, S. Harayama, Predominant growth of *Alcanivorax* strains in oil-contaminated and nutrient-supplemented sea water. *Environ. Microbiol.* **4**, 141–147 (2002).

3. A. Hara, K. Syutsubo, S. Harayama, *Alcanivorax* which prevails in oil-contaminated seawater exhibits broad substrate specificity for alkane degradation. *Environ. Microbiol.* **5**, 746–753 (2003).

4. W. F. M. Röling, M. G. Milner, D. M. Jones, F. Fratepietro, R. P. J. Swannell, F. Daniel, I. M. Head, Bacterial community dynamics and hydrocarbon degradation during a field-scale evaluation of bioremediation on a mudflat beach contaminated with buried oil. *Appl. Environ. Microbiol.* **70**, 2603–2613 (2004).

5. R. M. Atlas, T. C. Hazen, Oil biodegradation and bioremediation: a tale of the two worst spills in U.S. history. *Environ. Sci. Technol.* **45**, 6709–6715 (2011).

6. S. Schneiker, V. A. Martins dos Santos, D. Bartels, T. Bekel, M. Brecht, J. Buhrmester, T. N. Chernikova, R. Denaro, M. Ferrer, C. Gertler, A. Goesmann, O. V. Golyshina, F. Kaminski, A. N. Khachane, S. Lang, B. Linke, A. C. McHardy, F. Meyer, T. Nechitaylo, A. Pühler, D. Regenhardt, O. Rupp, J. S. Sabirova, W. Selbitschka, M. M. Yakimov, K. N. Timmis, F. J. Vorhölter, S. Weidner, O. Kaiser, P. N. Golyshin, Genome sequence of the ubiquitous hydrocarbon-degrading marine bacterium *Alcanivorax borkumensis*. *Nat. Biotechnol.* **24**, 997–1004 (2006).

7. T. C. Hazen, E. A. Dubinsky, T. Z. DeSantis, G. L. Andersen, Y. M. Piceno, N. Singh, J. K. Jansson, A. Probst, S. E. Borglin, J. L. Fortney, W. T. Stringfellow, M. Bill, M. E. Conrad, L. M. Tom, K. L. Chavarria, T. R. Alusi, R. Lamendella, D. C. Joyner, C. Spier, J. Baelum, M. Auer, M. L. Zemla, R. Chakraborty, E. L. Sonnenthal, P. D'haeseleer, H.-Y. N. Holman, S. Osman, Z. Lu, J. D. Van Nostrand, Y. Deng, J. Zhou, O. U. Mason, Deep-sea oil plume enriches indigenous oil-degrading bacteria. *Science*. **330**, 204–208 (2010).

8. F. Mapelli, A. Scoma, G. Michoud, F. Aulenta, N. Boon, S. Borin, N. Kalogerakis, D. Daffonchio, Biotechnologies for Marine Oil Spill Cleanup: Indissoluble Ties with Microorganisms. *Trends Biotechnol.* **35**, 860–870 (2017).

9. M. M. Yakimov, P. N. Golyshin, S. Lang, E. R. Moore, W. R. Abraham, H. Lünsdorf, K. N. Timmis, Alcanivorax borkumensis gen. nov., sp. nov., a new, hydrocarbon-degrading and surfactant-producing marine bacterium. *Int. J. Syst. Bacteriol.* **48 Pt 2**, 339–348 (1998).

10. L. Hall-Stoodley, J. W. Costerton, P. Stoodley, Bacterial biofilms: from the natural environment to infectious diseases. *Nat. Rev. Microbiol.* **2**, 95–108 (2004).

11. J. K. Teschler, D. Zamorano-Sánchez, A. S. Utada, C. J. Warner, G. C. Wong, R. G. Linington, F. H. Yildiz, Living in the matrix: assembly and control of *Vibrio cholerae* biofilms. *Nat. Rev. Microbiol.* **13**, 255–268 (2015).

12. R. M. Donlan, Biofilms: microbial life on surfaces. *Emerging Infect. Dis.* **8**, 881–890 (2002).

13. J. Tremblay, E. Yergeau, N. Fortin, S. Cobanli, M. Elias, T. L. King, K. Lee, C. W. Greer, Chemical dispersants enhance the activity of oil- and gas condensate-degrading marine bacteria. *ISME J.* **11**, 2793–2808 (2017).

14. O. U. Mason, T. C. Hazen, S. Borglin, P. S. G. Chain, E. A. Dubinsky, J. L. Fortney, J. Han, H.-Y. N. Holman, J. Hultman, R. Lamendella, R. Mackelprang, S. Malfatti, L. M. Tom, S. G. Tringe, T. Woyke, J. Zhou, E. M. Rubin, J. K. Jansson, Metagenome, metatranscriptome and single-cell sequencing reveal microbial response to Deepwater Horizon oil spill. *ISME J.* **6**, 1715–1727 (2012).

15. J. S. Sabirova, T. N. Chernikova, K. N. Timmis, P. N. Golyshin, Niche-specificity factors of a marine oil-degrading bacterium *Alcanivorax borkumensis* SK2. *FEMS Microbiol. Lett.* **285**, 89–96 (2008).

16. P. A. Rühs, L. Böcker, R. F. Inglis, P. Fischer, Studying bacterial hydrophobicity and biofilm formation at liquid–liquid interfaces through interfacial rheology and pendant drop tensiometry. *Colloids and Surfaces B: Biointerfaces*. **117**, 174–184 (2014).

17. G. Subbiahdoss, E. Reimhult, Biofilm formation at oil-water interfaces is not a simple function of bacterial hydrophobicity. *Colloids Surf. B Biointerfaces*. **194**, 111163 (2020).

18. L. Vaccari, D. B. Allan, N. Sharifi-Mood, A. R. Singh, R. L. Leheny, K. J. Stebe, Films of bacteria at interfaces: three stages of behaviour. *Soft Matter*. **11**, 6062–6074 (2015).

19. R. Grimaud, in *Handbook of hydrocarbon and lipid microbiology*, K. N. Timmis, Ed. (Springer Berlin Heidelberg, Berlin, Heidelberg, 2010), pp. 1491–1499.

20. M. P. Godfrin, M. Sihlabela, A. Bose, A. Tripathi, Behavior of marine bacteria in clean environment and oil spill conditions. *Langmuir*. **34**, 9047–9053 (2018).

21. C. Joannis-Cassan, M. Delia, J. Riba, Limitation phenomena induced by biofilm formation during hydrocarbon biodegradation. *Journal of Chemical Technology and Biotechnology*. **80**, 99–106 (2005).

22. N. K. Dewangan, J. C. Conrad, Adhesion of *Marinobacter hydrocarbonoclasticus* to Surfactant-Decorated Dodecane Droplets. *Langmuir*. **34**, 14012–14021 (2018).

23. V. Hickl, G. Juarez, Tubulation and dispersion of oil by bacterial growth on droplets. *Soft Matter*. **18**, 7217–7228 (2022).

24. R. Dangla, S. Lee, C. N. Baroud, Trapping microfluidic drops in wells of surface energy. *Phys. Rev. Lett.* **107**, 124501 (2011).

25. K. Drescher, J. Dunkel, C. D. Nadell, S. van Teeffelen, I. Grnja, N. S. Wingreen, H. A. Stone, B. L. Bassler, Architectural transitions in *Vibrio cholerae* biofilms at single-cell resolution. *Proc. Natl. Acad. Sci. USA*. **113** (2016), doi:10.1073/pnas.1601702113.

26. O. J. Meacock, A. Doostmohammadi, K. R. Foster, J. M. Yeomans, W. M. Durham, Bacteria solve the problem of crowding by moving slowly. *Nat. Phys.* **17**, 205–210 (2021).

27. J. Nijjer, C. Li, Q. Zhang, H. Lu, S. Zhang, J. Yan, Mechanical forces drive a reorientation cascade leading to biofilm self-patterning. *Nat. Commun.* **12**, 6632 (2021).

28. K. Copenhagen, R. Alert, N. S. Wingreen, J. W. Shaevitz, Topological defects promote layer formation in *Myxococcus xanthus* colonies. *Nat. Phys.* (2020), doi:10.1038/s41567-020-01056-4.

29. L. Metselaar, J. M. Yeomans, A. Doostmohammadi, Topology and Morphology of Self-Deforming Active Shells. *Phys. Rev. Lett.* **123**, 208001 (2019).

30. L. A. Hoffmann, L. N. Carenza, J. Eckert, L. Giomi, Theory of defect-mediated morphogenesis. *Sci. Adv.* **8**, eabk2712 (2022).

31. K. Kawaguchi, R. Kageyama, M. Sano, Topological defects control collective dynamics in neural progenitor cell cultures. *Nature*. **545**, 327–331 (2017).

32. P. Guillamat, C. Blanch-Mercader, G. Pernollet, K. Kruse, A. Roux, Integer topological defects organize stresses driving tissue morphogenesis. *Nat. Mater.* **21**, 588–597 (2022).

33. Y. Maroudas-Sacks, L. Garion, L. Shani-Zerbib, A. Livshits, E. Braun, K. Keren, Topological defects in the nematic order of actin fibres as organization centres of Hydra morphogenesis. *Nat. Phys.* **17**, 251–259 (2021).

34. T. B. Saw, A. Doostmohammadi, V. Nier, L. Kocgozlu, S. Thampi, Y. Toyama, P. Marcq, C. T. Lim, J. M. Yeomans, B. Ladoux, Topological defects in epithelia govern cell death and extrusion. *Nature*. **544**, 212–216 (2017).

35. A. Passeri, M. Schmidt, T. Haffner, V. Wray, S. Lang, F. Wagner, Marine biosurfactants. IV. Production, characterization and biosynthesis of an anionic glucose lipid from the marine bacterial strain MM1. *Applied Microbiology and Biotechnology*. **37**, 281–286 (1992).

36. N. L. Olivera, M. L. Nievas, M. Lozada, G. Del Prado, H. M. Dionisi, F. Siñeriz, Isolation and characterization of biosurfactant-producing Alcanivorax strains: hydrocarbon accession strategies and alkane hydroxylase gene analysis. *Res. Microbiol.* **160**, 19–26 (2009).

37. L. S. Dorobantu, A. K. C. Yeung, J. M. Foght, M. R. Gray, Stabilization of oil-water emulsions by hydrophobic bacteria. *Appl. Environ. Microbiol.* **70**, 6333–6336 (2004).

38. D. Vella, P. Aussillous, L. Mahadevan, Elasticity of an interfacial particle raft. *Europhysics Letters*. **68**, 212–218 (2004).

39. H. H. Tuson, G. K. Auer, L. D. Renner, M. Hasebe, C. Tropini, M. Salick, W. C. Crone, A. Gopinathan, K. C. Huang, D. B. Weibel, Measuring the stiffness of bacterial cells from growth rates in hydrogels of tunable elasticity. *Mol. Microbiol.* **84**, 874–891 (2012).

40. J. W. Cahn, Phase separation by spinodal decomposition in isotropic systems. *J. Chem. Phys.* **42**, 93–99 (1965).

41. F. Jülicher, A. Ajdari, J. Prost, Modeling molecular motors. *Rev. Mod. Phys.* **69**, 1269–1282 (1997).

42. G. Salbreux, J. Prost, J. F. Joanny, Hydrodynamics of cellular cortical flows and the formation of contractile rings. *Phys. Rev. Lett.* **103**, 058102 (2009).

43. P. G. de Gennes, J. Prost, *The Physics Of Liquid Crystals (International Series Of Monographs On Physics)* (Oxford University Press, U.S.A., ed. 2, 1995).

44. J. R. Frank, M. Kardar, Defects in nematic membranes can buckle into pseudospheres. *Phys. Rev. E Stat. Nonlin. Soft Matter Phys.* **77**, 041705 (2008).

45. O. Shishkov, M. Hu, C. Johnson, D. L. Hu, Black soldier fly larvae feed by forming a fountain around food. *Journal of The Royal Society Interface*. **16**, 20180735 (2019).

46. T. C. Hazen, R. C. Prince, N. Mahmoudi, Marine Oil Biodegradation. *Environ. Sci. Technol.* **50**, 2121–2129 (2016).

47. G. Salbreux, F. Jülicher, J. Prost, A. Callan-Jones, Theory of nematic and polar active fluid surfaces. *arXiv* (2022), doi:10.48550/arxiv.2201.09251.

48. J. Liu, A. Prindle, J. Humphries, M. Gabalda-Sagarra, M. Asally, D. D. Lee, S. Ly, J. Garcia-Ojalvo, G. M. Süel, Metabolic co-dependence gives rise to collective oscillations within biofilms. *Nature*. **523**, 550–554 (2015).

REFERENCES (Supplementary Materials)

1. M. M. Yakimov, P. N. Golyshin, S. Lang, E. R. Moore, W. R. Abraham, H. Lünsdorf, K. N. Timmis, Alcanivorax borkumensis gen. nov., sp. nov., a new, hydrocarbon-degrading and surfactant-producing marine bacterium. *Int. J. Syst. Bacteriol.* **48 Pt 2**, 339–348 (1998).

2. M. Prasad, N. Obana, K. Sakai, T. Nagakubo, S. Miyazaki, M. Toyofuku, J. Fattaccioli, N. Nomura, A. S. Utada, Point Mutations Lead to Increased Levels of c-di-GMP and Phenotypic Changes to the Colony Biofilm Morphology in. *Microbes and Environments*. **34**, 104–107 (2019).

3. A. Rotem, A. R. Abate, A. S. Utada, V. Van Steijn, D. A. Weitz, Drop formation in non-planar microfluidic devices. *Lab Chip*. **12**, 4263–4268 (2012).

4. T. Trantidou, Y. Elani, E. Parsons, O. Ces, Hydrophilic surface modification of PDMS for droplet microfluidics using a simple, quick, and robust method via PVA deposition. *Microsyst. Nanoeng.* **3**, 16091 (2017).

5. R. Dangla, S. Lee, C. N. Baroud, Trapping microfluidic drops in wells of surface energy. *Phys. Rev. Lett.* **107**, 124501 (2011).

6. T. D. Dimitrova, F. Leal-Calderon, Forces between Emulsion Droplets Stabilized with Tween 20 and Proteins. *Langmuir*. **15**, 8813–8821 (1999).

7. T. Kunoh, K. Morinaga, S. Sugimoto, S. Miyazaki, M. Toyofuku, K. Iwasaki, N. Nomura, A. S. Utada, Polyfunctional Nanofibril Appendages Mediate Attachment, Filamentation, and Filament Adaptability in Leptothrix cholodnii. *ACS Nano*. **14**, 5288–5297 (2020).

8. W. R. Abraham, H. Meyer, M. Yakimov, Novel glycine containing glucolipids from the alkane using bacterium *Alcanivorax borkumensis*. *Biochimica Et Biophysica Acta-Lipids and Lipid Metabolism*. **1393**, 57–62 (1998).

9. A. Passeri, M. Schmidt, T. Haffner, V. Wray, S. Lang, F. Wagner, Marine biosurfactants. IV. Production, characterization and biosynthesis of an anionic glucose lipid from the marine bacterial strain MM1. *Applied Microbiology and Biotechnology*. **37**, 281–286 (1992).

10. M. P. Kem, H. K. Zane, S. D. Springer, J. M. Gauglitz, A. Butler, Amphiphilic siderophore production by oil-associating microbes. *Metallomics*. **6**, 1150–1155 (2014).

11. J. S. Sabirova, T. N. Chernikova, K. N. Timmis, P. N. Golyshin, Niche-specificity factors of a marine oil-degrading bacterium *Alcanivorax borkumensis* SK2. *FEMS Microbiol. Lett.* **285**, 89–96 (2008).

12. P.-G. De Gennes, F. Brochard-Wyart, D. Quéré, *Capillarity and wetting phenomena: drops, bubbles, pearls, waves* (Springer, 2004), vol. 315.

13. L. S. Dorobantu, A. K. C. Yeung, J. M. Foght, M. R. Gray, Stabilization of oil-water emulsions by hydrophobic bacteria. *Appl. Environ. Microbiol.* **70**, 6333–6336 (2004).

14. R. J. Neufeld, J. E. Zajic, D. F. Gerson, Cell surface measurements in hydrocarbon and carbohydrate fermentations. *Appl. Environ. Microbiol.* **39**, 511–517 (1980).

15. B. J. Place, M. J. Perkins, E. Sinclair, A. L. Barsamian, P. R. Blakemore, J. A. Field, Trace analysis of surfactants in corexit oil dispersant formulations and seawater. *Deep Sea Res Part 2 Top Stud Oceanogr*. **129**, 273–281 (2016).

16. S. K. Nayar, Y. Nakagawa, Shape from Focus. *IEEE Transactions on Pattern Analysis and Machine Intelligence*. **16**, 824–831 (1994).

17. S. Pertuz, D. Puig, M. A. Garcia, Analysis of focus measure operators for shape-from-focus. *Pattern Recognit.* **46**, 1415–1432 (2013).

18. O. J. Meacock, A. Doostmohammadi, K. R. Foster, J. M. Yeomans, W. M. Durham, Bacteria solve the problem of crowding by moving slowly. *Nat. Phys.* **17**, 205–210 (2021).

19. S. Pertuz, D. Puig, M. A. Garcia, A. Fusiello, Generation of all-in-focus images by noise-robust selective fusion of limited depth-of-field images. *IEEE Trans. Image Process.* **22**, 1242–1251 (2013).

20. G. Duclos, R. Adkins, D. Banerjee, M. S. E. Peterson, M. Varghese, I. Kolvin, A. Baskaran, R. A. Pelcovits, T. R. Powers, A. Baskaran, F. Toschi, M. F. Hagan, S. J. Streichan, V. Vitelli, D. A. Beller, Z. Dogic, Topological structure and dynamics of three-dimensional active nematics. *Science*. **367**, 1120–1124 (2020).

21. K. Kawaguchi, R. Kageyama, M. Sano, Topological defects control collective dynamics in neural progenitor cell cultures. *Nature*. **545**, 327–331 (2017).

22. I. Derényi, F. Jülicher, J. Prost, Formation and interaction of membrane tubes. *Phys. Rev. Lett.* **88**, 238101 (2002).

23. G. Salbreux, F. Jülicher, J. Prost, A. Callan-Jones, Theory of nematic and polar active fluid surfaces. *arXiv* (2022), doi:10.48550/arxiv.2201.09251.

24. J. F. Joanny, K. Kruse, J. Prost, S. Ramaswamy, The actin cortex as an active wetting layer. *Eur. Phys. J. E Soft Matter*. **36**, 52 (2013).

25. F. Jülicher, A. Ajdari, J. Prost, Modeling molecular motors. *Rev. Mod. Phys.* **69**, 1269–1282 (1997).

26. J. Ranft, M. Basan, J. Elgeti, J.-F. Joanny, J. Prost, F. Jülicher, Fluidization of tissues by cell division and apoptosis. *Proc Natl Acad Sci USA*. **107**, 20863–20868 (2010).

27. B. Palmieri, Y. Bresler, D. Wirtz, M. Grant, Multiple scale model for cell migration in monolayers: Elastic mismatch between cells enhances motility. *Sci. Rep.* **5**, 11745 (2015).

28. L. A. Hoffmann, L. N. Carenza, J. Eckert, L. Giomi, Theory of defect-mediated morphogenesis. *Sci. Adv.* **8**, eabk2712 (2022).

29. J. R. Frank, M. Kardar, Defects in nematic membranes can buckle into pseudospheres. *Phys. Rev. E Stat. Nonlin. Soft Matter Phys.* **77**, 041705 (2008).

606
607
608

FIGURES

609
610

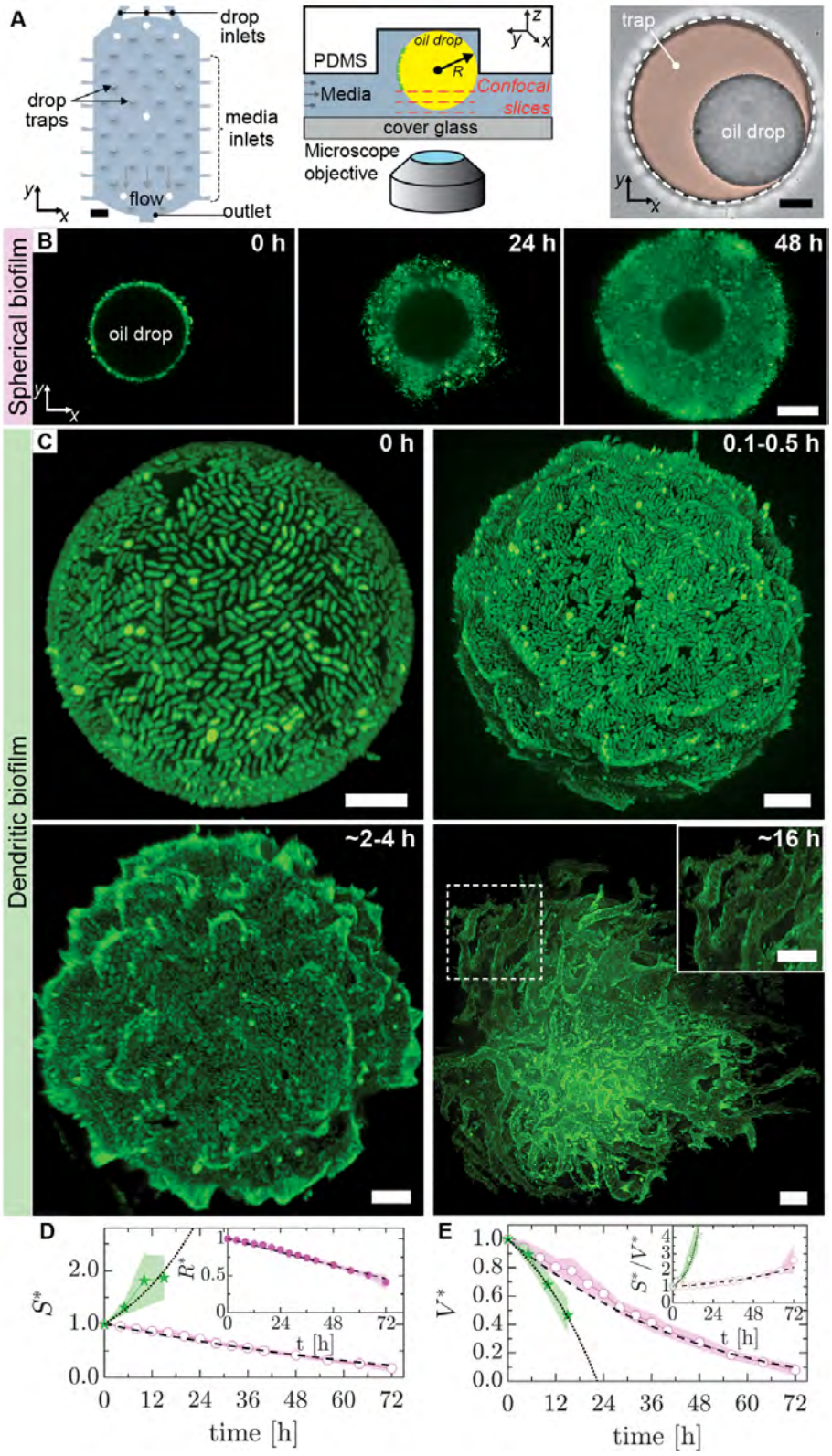

611
612

Fig. 1

613

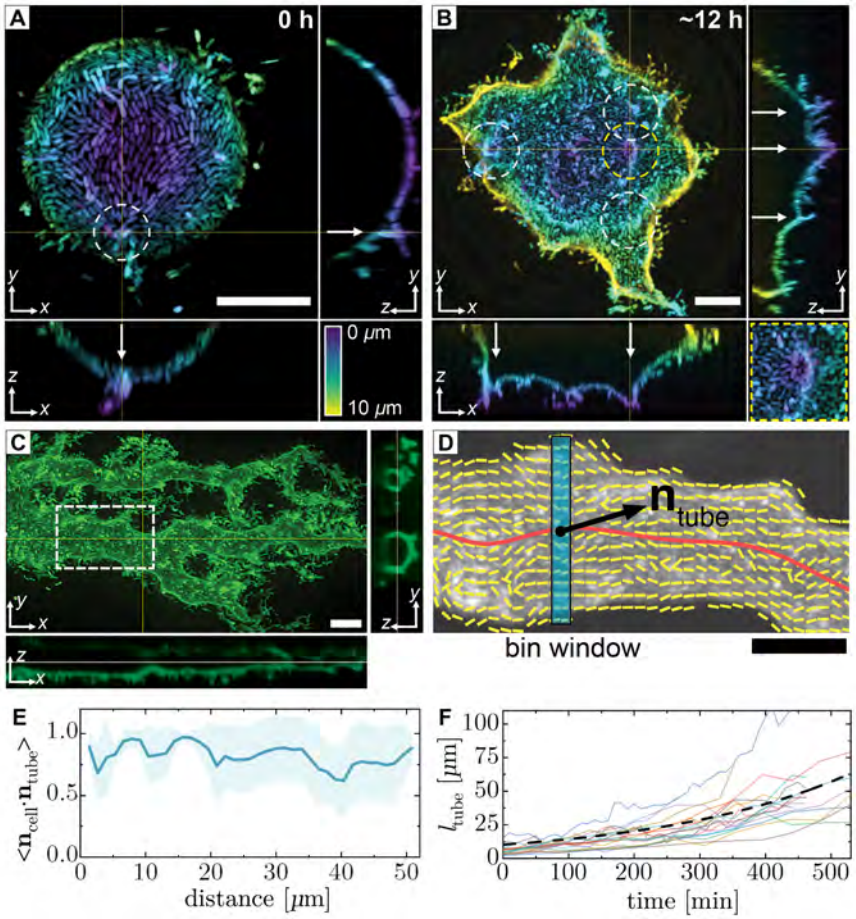
A
0 h
B
~12 h
0 μm
10 μm
C
D
n tube
bin window
E
<n cell·n tube>
distance [μm]
F
l tube [μm]
time [min]

Fig. 2

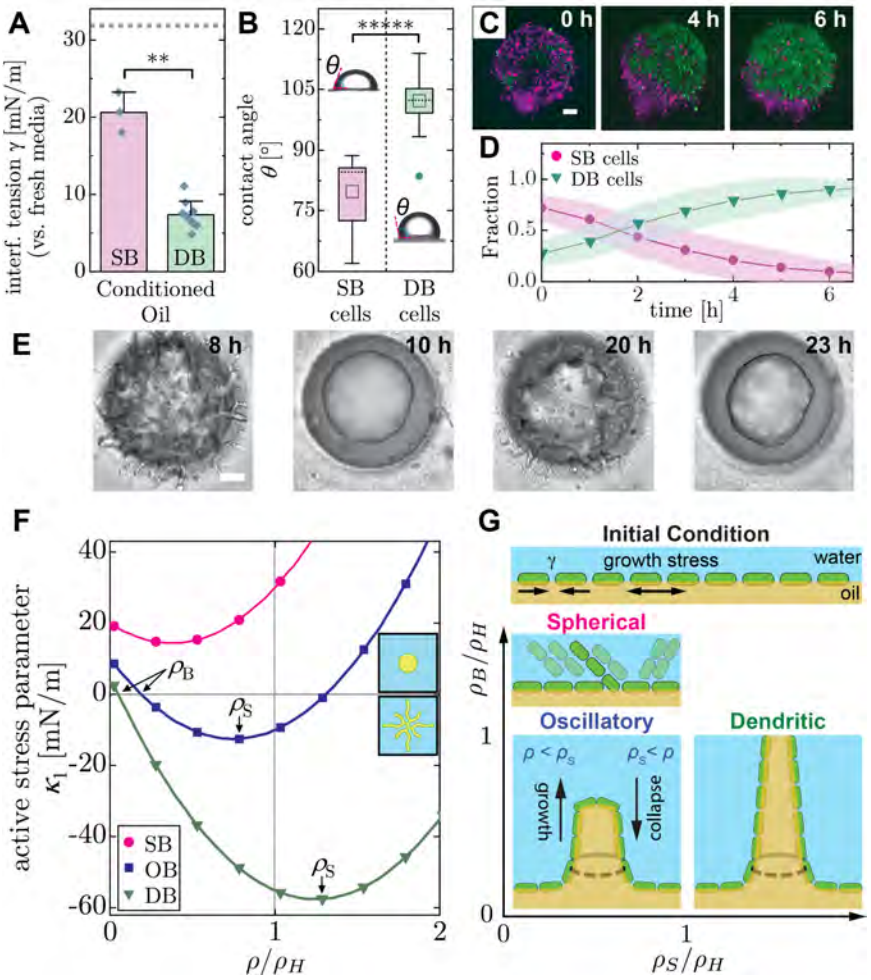
A
interf. tension γ [mN/m] (vs. fresh media)
SB
DB
Conditioned Oil
B
contact angle θ [°]
SB cells
DB cells
C
0 h
4 h
6 h
D
SB cells
DB cells
Fraction
time [h]
E
8 h
10 h
20 h
23 h
F
active stress parameter κ1 [mN/m]
ρ/ρH
SB
OB
DB
G
Initial Condition
γ
growth stress
water
oil
Spherical
Oscillatory
Dendritic
growth
collapse
ρB/ρH
ρS/ρH

Fig. 3

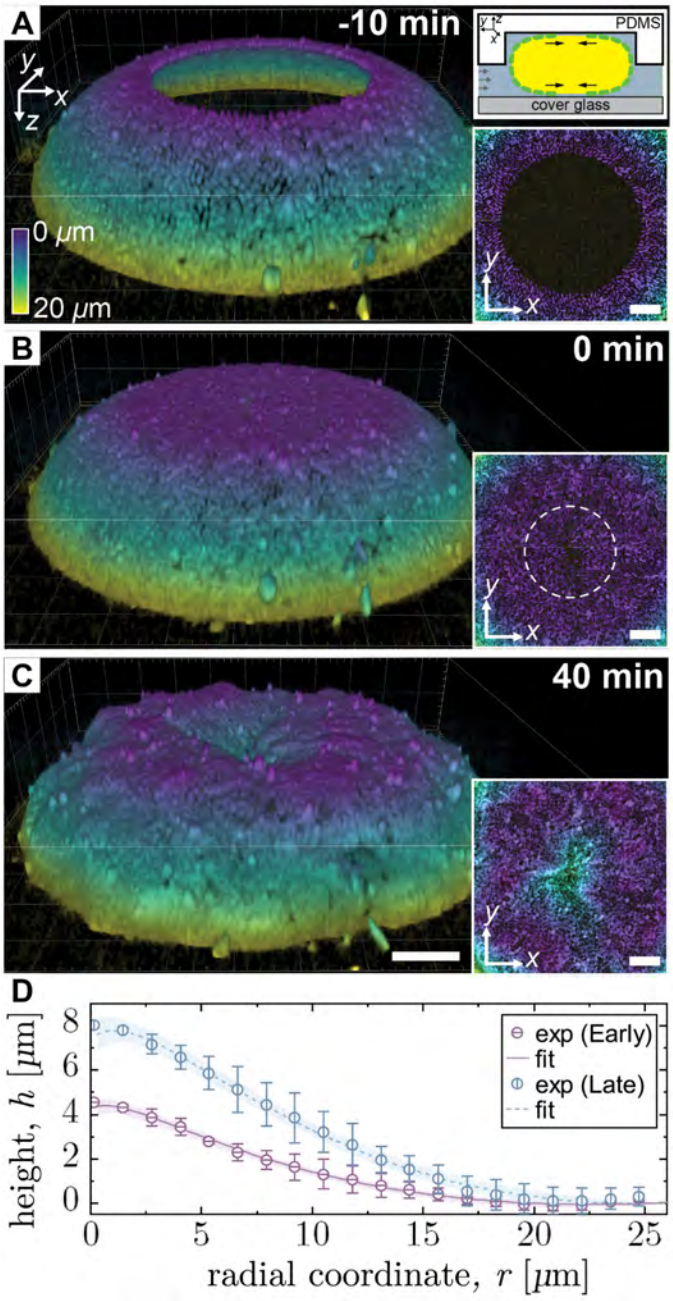
A
-10 min
PDMS
cover glass
0 μm
20 μm
B
0 min
C
40 min
D
exp (Early)
fit
exp (Late)
fit
height, h [μm]
radial coordinate, r [μm]

Fig. 4

FIGURE CAPTIONS

Fig. 1: Spherical and dendritic biofilm phenotypes on oil drops in a microfluidic trap. (A) Schematic of the microfluidic oil-drop trap device showing media-filled channels. Oil drops are trapped in the raised circular regions. Inlets on either side of the drop chamber connect to reservoirs that provide a gentle flow of media through the trap chamber. The white circles are pillars. Scale bar = 200 μm. (*center*) Schematic cross-section of an individual trap. (*right*) Bright-field image of a representative drop in a trap. The trap is outlined with a white dashed line, while the pocket is colored orange as a guide for the eye. Scale bar = 20 μm. (B) Representative time-lapse sequence of confocal images showing the development of the spherical biofilm (SB) phenotype. As the biofilm (green) grows, the oil droplet (central void) shrinks. Scale bar = 10 μm. (C) Maximum intensity projection confocal images showing the development of the dendritic biofilm (DB) phenotype on representative drops. Local nematic order is present at confluence (~0 h), buckling (0.1-0.5 h) and protrusions (2-4 h) appear later, and large-scale remodeling of the interface leading to the formation of tubes occurs much later (16 h). Scale bar = 10 μm. (D,E) Normalized surface area (S^*) and volume (V^*) of oil drops as a function of time for (∘) SB and (⋆) DBs. The solid lines and filled regions denote the mean ± one standard deviation (±s.d.) (n_{SB} = 11 drops; n_{DB} = 12 drops). The dashed and dotted lines are best fits of our analytical models of oil degradation for SB and DB phenotypes, respectively (**Supplementary Information**). The filled symbols represent measurements, while open symbols are quantities calculated from measured values. S^* for SBs is estimated from the measured normalized drop radius (R^*), shown in the inset in (D). S^*/V^* as a function of time is shown in the inset of (E). R, S, and V are normalized by their initial values, respectively.

Fig. 2: Dendrites originate from topological defects. Confocal images of representative droplets (A) early (~0 h) and (B) later (~12 h) in biofilm development. The images are color coded by depth. The dashed circles enclose topological defects with a charge of +1, while the arrows indicate protrusions. (B, inset) A magnified view of the central defect circled in yellow. (C) Confocal image of a bacteria-covered tube connected to a deformed droplet with corresponding orthogonal views (~20 h). (D) Director field of the visible cells in the dashed box in (C). The director field (yellow lines), tube axis (red line), the local tangent unit vector ($\mathbf{n}_{tube}$) along the tube axis, and the bin window (blue) are shown. (E) Axial order of the cells along the oil tube shown in (D). For a sliding window of width 1.5 μm along the tube, the local axial order is defined as the average of the individual scalar products between the director-field unit vectors ($\mathbf{n}_{cell}$) and local tangent unit vectors. $<\mathbf{n}_{cell} \cdot \mathbf{n}_{tube}> = 1$ for parallel alignment and 0 for perpendicular alignment. The thick solid line and shaded region represents mean±s.d. (F) Oil tube length (l_{tube}) plotted as a function of time (n=18 tubes from three independent tests). The dashed line is a fit to the average tube length using an exponential equation (adjusted R-square = 0.96). All scale bars = 10 μm.

Fig. 3: Theoretical model of tubulation. (A) Interfacial tension (γ) between biofilm-conditioned oil and fresh media measured using pendant drop tensiometry for spherical (SB) and dendritic biofilms (DB), respectively (from n_{SB}=3 and n_{DB}=10 independent tests). The dashed line indicates γ between fresh oil and fresh medium ($n_{control}$=5). We used Welch's *t*-test to compare the means (** denotes p<0.01; p=0.0062). (B) Three-phase contact angles ($\boldsymbol{\theta}$) between a water drop deposited on a bacterial lawn of SB and DB phenotypes, submerged in oil. The (□) is the mean, the horizontal dashed lines are the medians, and (●) represents an outlier (from n_{SB}=10 and n_{DB}=13 independent tests). We used Welch's *t*-test to compare the means (***** denotes p<0.00001; p=1.2×10^{-6}). (inset) Images of the water drops wetting bacterial lawns that are submerged in oil. (C) Time-lapse sequence showing the competition between SB cells (magenta) and DB cells (green) for interfacial area on a trapped droplet. Droplets are generated in a suspension containing SB and DB cells at a ratio of 3:1 (see **Supplementary Information** for details). DB cells displace a monolayer of SB cells over the course of ~6 h. (D) Measurement of the fractional coverage of SB and DB as a function of time from confocal images. The solid line and filled regions represent mean ± s.d. (from n=10 representative drops). (E) Oscillatory biofilm (OB) behavior demonstrated by a culture sampled for an intermediate duration between the SB and DBs. (F) Model of the tension (κ_1 in the phase-field model) experienced by the tip of a tube as a function of normalized interfacial cell density (ρ/ρ_H) (see **Supplementary Information** for details). We normalize cell density by the homeostatic interfacial cell density (ρ_H). Positive (negative) values of κ_1 indicate tube retraction (expansion). For the SB phenotype, tension is positive for all densities, thus tubes are unable to form. For the intermediate OB phenotype, the homeostatic density is located in a regime where the tension is increasing as a function of biofilm density. As cell density approaches ρ_H, the increasing tension further compacts the cells, which further increases cell density, driving positive feedback that eventually triggers collapse of tube structures. The slope at the y-intercept is k_1 = 3, 6, and 10 for the SB, OB, and DB models, respectively. The ρ_B is the critical buckling density, where κ_1<0. For SBs, ρ_B=∞. The ρ_S is the optimal cell density, where κ_1 reaches a minimum, and beyond which the effect of spontaneous curvature is reduced. (insets) Phase-field simulation showing a circular droplet (κ_1>0) and a tubulated droplet (κ_1<0). (G) Schematic phase diagram of the biofilm phenotypes in terms of normalized densities: ρ_S/ρ_H and ρ_B/ρ_H. When ρ_B/ρ_H > 1, SBs form because the interfacial cell density can never become sufficiently large to induce buckling. For ρ_B/ρ_H < 1, cell division drives an increase in cell density beyond ρ_B. When ρ_S/ρ_H < 1, oscillations between the spherical and dendritic phenotypes can occur (OB). When, ρ_S/ρ_H > 1, stable dendrites (DB) occur.

Fig. 4: Defect mediated buckling of the surface of a confined droplet. (A-C) Time-lapse confocal image sequence showing the evolution of a dendritic biofilm on a 'flattened' drop, color coded by depth. (A) Prior to confluency (-10 min), interfacial tension excludes cells from the flattened regions at the top and bottom of the droplets. These regions are generated where the non-wetting droplets make contact with the glass floor and PDMS ceiling. See the (upper) inset for a droplet schematic and the (lower) inset for the top view of the droplet. (B) Confluent monolayer is formed at t_0 = 0 min (see inset and **Fig. S10**). (inset) Top view of droplet with a circle enclosing the location of the nematic defect. (C) Dimple formation in the droplet at the defect. All scale bars = 10 μm. (D) Evolution of the dimple height (h) from xy-line profiles measured across the droplet midplane, at 20 min (early) and 26 ± 3 min (late) post-confluency. Dimple height is shown as a function of the radial coordinate (r). The fits to the data are based on **Eq. (2)**. The solid error bars and filled regions represent ±s.d on the experimental data and fits, respectively (see **Supplementary Information** for details on the fitting procedure and error estimation). Early-profile data are the average of the x- and y-profiles (n=4) at t = 20 min, while the late-profile data are the average of the x- and y-profiles binned at 23, 26, and 29 min (n=12), respectively. To generate the dimensional values shown, we rescale the non-dimensionalized h-values by the dimple heights, 4.5 μm and 8.0 μm at early and late times, respectively, while r is rescaled by 26 μm at all times.